

Closeby Habitable Exoplanet Survey (CHES). I. Astrometric Noise and Planetary Detection Efficiency due to Stellar Spots and Faculae

CHUNHUI BAO,^{1,2} JIANGHUI JI,^{1,2,3} DONGJIE TAN,^{1,2} GUO CHEN,^{1,2} XIUMIN HUANG,^{1,2} SU WANG,^{1,3} AND YAO DONG^{1,3}

¹*CAS Key Laboratory of Planetary Sciences, Purple Mountain Observatory, Chinese Academy of Sciences, Nanjing 210023, China; jjh@pmo.ac.cn*

²*School of Astronomy and Space Science, University of Science and Technology of China, Hefei 230026, China*

³*CAS Center for Excellence in Comparative Planetology, Hefei 230026, China*

Submitted to AAS Journal

ABSTRACT

The Closeby Habitable Exoplanet Survey (CHES) is dedicated to the astrometric exploration for habitable-zone Earth-like planets orbiting solar-type stars in close proximity, achieving unprecedented micro-arcsecond precision. Given the elevated precision, thorough consideration of photocenter jitters induced by stellar activity becomes imperative. This study endeavors to model the stellar activity of solar-type stars, compute astrometric noise, and delineate the detection limits of habitable planets within the astrometric domain. Simulations were conducted for identified primary targets of CHES, involving the generation of simulated observed data for astrometry and photometry, accounting for the impact of stellar activity. Estimation of activity levels in our samples was achieved through chromospheric activity indices, revealing that over 90% of stars exhibited photocenter jitters below 1 μ as. Notably, certain proximate stars, such as α Cen A and B, displayed more discernible noise arising from stellar activity. Subsequent tests were performed to evaluate detection performance, unveiling that stellar activity tends to have a less pronounced impact on planetary detectability for the majority of stars. Approximately 95% of targets demonstrated a detection efficiency exceeding 80%. However, for several cold stars, e.g., HD 32450 and HD 21531, with the habitable zones close to the stars, a reduction in detection efficiency was observed. These findings offer invaluable insights into the intricate interplay between stellar activity and astrometric precision, significantly advancing our understanding in the search for habitable planets.

Keywords: astrometry - stars: activity - stars: solar-type - planetary systems - planets and satellites: detection

1. INTRODUCTION

Over several decades, the discovery of more than 5500 exoplanets has been achieved through the application of diverse methods¹. The predominant techniques employed for these discoveries are the transit and radial velocity (RV) methods. However, these two approaches are susceptible to the impact of stellar activity, capable of inducing RV variations akin to those attributed to orbiting planets. With the development of the new generation of extreme-precision spectrographs, the radial-velocity (RV) measurement at sub-meter-per-

second precision becomes feasible, including the Echelle SPectrograph for Rocky Exoplanets and Stable Spectroscopic Observations (ESPRESSO) (Pepe et al. 2010), the EXtreme PREcision Spectrograph (EXPRES) (Jurgenson et al. 2016) and NEID (Lin et al. 2022). The previous investigations showed that the amplitude of RV variations resulting from stellar activity ranges in the order of a few m/s (Hatzes 2002; Lagrange et al. 2010; Butler et al. 2006, 2017; Laliotis et al. 2023). The dispersion in radial velocity due to granulation is estimated to be larger than 0.3 m/s, significantly surpassing the signals emanating from terrestrial planets (approximately ~ 0.09 m/s). Zhao et al. (2022) reported that EXPRES is unable to detect Earth-like planets in the presence of stellar variability. Periodic variability in stellar activity

¹ <https://exoplanetarchive.ipac.caltech.edu>

can mimic a planetary transit signal, leading to potential false positives (Lanza et al. 2009). Photometry observations are also influenced by stellar oscillations and granulation, which are comparable to the planetary signal at the precision of CHEOPS (CHAracterising ExOPlanet Satellite) and ESPRESSO (Sulis et al. 2023). The simulations of PLATO (PLANetary Transits and Oscillations of stars) concluded that the noise due to granulation is about 100 ppm (Morris et al. 2020), comparable to the depth of Earth-like planets. Despite efforts to bolster the performance of the RV method through denoising techniques such as Gaussian processes and extended observational durations (spanning ten years), uncertainties in mass estimations persistently exceed 30% (Meunier et al. 2023).

The astrometric method offers distinct advantages in the detection of terrestrial planets. Several astrometric missions, among them the Gaia satellite, have made exoplanet detection a primary scientific objective. Notably, the discovery of over 60 Jupiter-mass planets through astrometry was reported in Gaia DR3 (Gaia Collaboration et al. 2023). Numerous upcoming missions are specifically dedicated to the search for Earth-like planets, including Theia mission (The Theia Collaboration et al. 2017), the Closeby Habitable Exoplanet Survey (CHES) mission (Ji et al. 2022), Small-JASMINE mission (Kawata et al. 2023), and the Nancy Grace Roman Telescope (Gandhi et al. 2023), Habitable Worlds Observatory (HWO) survey (Mamajek & Stapelfeldt 2024). For instance, Theia endeavors to identify approximately six habitable terrestrial planets, a breakthrough with profound implications for understanding the conditions conducive to planetary formation and the emergence of life (The Theia Collaboration et al. 2017).

The meticulous consideration of stellar activity noise proves indispensable when operating at ultra-high precision. Predominantly, the primary astrometric shifts arise from the intricate interplay of stellar spots and faculae. Stellar spots, magnetic structures that manifest as darkened regions on the stellar surface, comprise a darker core called the umbra, surrounded by a slightly bright halo known as the penumbra (Solanki 2003). Faculae, existing in proximity to spots, exhibit a slightly higher temperature than the photosphere. Consequently, while facular contrast in temperature is less pronounced compared to spots, their significantly larger areas contribute crucially to astrometric shifts.

Considerable investigation has been dedicated to the intricate task of modeling astrometric jitter induced by spots, particularly in anticipation of the Space Interferometry Mission (SIM) (Eriksson & Lindgren 2007; Makarov et al. 2009, 2010). Their findings suggested the

feasibility of detecting Earth-like planets around quiescent stars analogous to the Sun. However, challenges arise when dealing with more active stars. Lagrange et al. (2011) extended their considerations to encompass both plages and spots, utilizing solar spots groups and bright structures from USAF/NOAA and MDI/SOHO and revealed that the amplitude of activity-induced astrometric signals remains below $0.2 \mu\text{as}$.

Based on their model, Meunier et al. (2019) incorporated granulation and chromospheric emission, extending the spectral type to F6-K4 stars. They determined that the root mean square (rms) of the astrometric activity time series for other main-sequence stars can be two to five times the solar value. Nevertheless, the detection rates for habitable terrestrial planets persist above 50%, marking a substantial improvement compared to the RV method (Meunier et al. 2020). In their analysis of simulated time series, Meunier & Lagrange (2022) concentrated on 55 nearby stars in the Theia sample. Their findings echoed similar conclusions, suggesting that stellar activity minimally impacts the detection of planets for solar-type stars, except for the closest stars α Cen A and B. They also emphasized the need to enhance the observation strategy for certain subgiants due to the more distant habitable zone. Additionally, studies based on Gaia accuracy, such as Morris et al. (2018), developed a model attributing stellar jitter to spots and concluded that Gaia’s precision is adequate to measure photocenter jitter for some M dwarfs within 10 pc.

In a recent study, Shapiro et al. (2021) computed the displacements observable in both the Gaia and Small-JASMINE passbands (Kawata et al. 2023). Notably, they identified a jitter amplitude in the G-band of approximately $0.5 \mu\text{as}$ for Sun located at 10 pc, anticipated to be twice as large as that in the Small-JASMINE near-infrared passbands. Expanding their investigation to stars observed at diverse inclinations, metallicity levels, and active-region nesting degrees (Sowmya et al. 2021), they discovered that astrometric shifts peak at an intermediate inclination in the Gaia-G band. Building upon the understanding that active magnetic structures tend to emerge in higher latitude regions (Strassmeier 2009), Sowmya et al. (2022) advanced their research by exploring stars with solar fundamental parameters but faster rotation than the Sun. Their findings indicated that magnetic jitter is predominantly spot-dominated for rapid rotators. In an exploration of the multi-wavelength strategy in astrometry, Kaplan-Lipkin et al. (2022) employed solar simulations across five distinct passbands based on Shapiro et al. (2021). Their results highlighted that the minimum detectable mass, through a combination of observations like Gaia G and

R bands, is 0.005 Earth mass. However, it is crucial to note that their assumptions involved perfect instruments, which can introduce much larger noise than stellar activity in practical scenarios.

The primary goal of this work is to evaluate the impact of stellar activity on the astrometric signal of the target stars of CHES. We developed a model that incorporates spots and faculae to simulate stellar activity in astrometry. The stellar activity levels were derived from photometric data obtained from TESS and the chromospheric index $\log R'_{\text{HK}}$. Subsequently, we generated simulated astrometric time series for each target. Noteworthy, we observed that nearly 75% of stars exhibit minimal photocenter jitter, with standard deviations lower than $0.24 \mu\text{as}$. Moreover, we introduced simulated habitable planets and conducted retrieval experiments to ascertain their mass and period. The retrieval performance proved to be satisfactory, with approximately 80% of simulated planets around nearly 95% of the stars being successfully recovered in our assessments. These findings underscore the feasibility of the astrometry method for detecting terrestrial planets, even when considering the noise introduced by stellar activity.

The paper is structured as follows: Section 2 provides a brief description of the properties of targets and planets. In Section 3, we elaborate on the stellar activity model, delineate the properties of spots and faculae, and elucidate the procedure for generating simulated stellar jitter at each time step. The methodology employed to estimate the detection efficiency of stars is outlined in Section 4. Subsequently, Section 5 presents the outcomes of simulations and the detection efficiency. In the final section, we summarize the major results.

2. TARGETS AND APPROACH

2.1. CHES satellite

The Closeby Habitable Exoplanet Survey (CHES) mission is set forth to unveil habitable-zone Earth-like planets surrounding solar-type stars in close proximity, approximately 10 parsecs distant from our solar system with micro-arcsecond relative astrometry techniques. The primary scientific objectives of CHES encompass the detection of Earth Twins or terrestrial planets within habitable zones orbiting 100 FGK nearby stars (Ji et al. 2022). Moreover, the mission aims to execute an exhaustive survey and intricately characterize the neighboring planetary systems, and reveal the real planetary masses and 3-dimensional orbits that provide crucial clues to their planetary formation and dynamical evolution (Youdin & Goodman 2005; Johansen et al. 2007; Jin et al. 2016; Huang et al. 2019; Liu et al. 2019; Pan et al. 2022, 2024). CHES is expected to enrich the

sample of Earth-like planets, which helps to comprehensively understand the formation and evolution of planetary systems (Ida & Lin 2004; Mordasini et al. 2012; Jin et al. 2014; Liu & Ji 2020; Huang & Ji 2022; Huang et al. 2023). The CHES satellite, outfitted with a 1.2-meter aperture high-quality telescope featuring low distortion and high stability, will be stationed at the Sun-Earth L2 point, continuously observing all target stars over a 5-year duration (Ji et al. 2022). Within a planetary system, the host star undergoes a subtle wobble around the common center of mass, typically demonstrating an amplitude of $0.3 \mu\text{as}$, which is measured for a solar-mass star situated at a distance of 10 parsecs, influenced by an Earth-mass planet located at 1 AU. In the astrometry, our measurements are focused on the position of the stellar photocenter, operating under the assumption that it coincides with the center of mass. However, beyond the gravitational influence of planets, the stellar photocenter can experience displacement due to the magnetic activity of the host star. Bright faculae regions contribute to increased brightness and attract the photocenter, while dark spots exert the opposite effect. The resulting photocenter jitters are measured in milli stellar radii, a scale comparable to the astrometric signature of an Earth-like planet (Catanzarite et al. 2008).

2.2. Target Selection

In this study, we have identified 94 main sequence stars from the CHES targets catalogue. The distribution of effective temperature and luminosity is illustrated in Figure 1, with colors denoting the stellar types (e.g., F, G, K). Remarkably, the majority of these stars are positioned within approximately 10 pc from the solar system. Additionally, the astrophysical parameters of the target stars are derived primarily from the TIC8.2 input catalogue (Paegert et al. 2021) and are succinctly presented in the appendix.

2.3. Planetary signals

The primary scientific goal of CHES is to detect the habitable planets orbiting nearby solar-type stars by observing the stellar wobbles induced by planetary gravity. The amplitude of the astrometric signal produced by a planet can be described as (Perryman et al. 2014):

$$\begin{aligned} \alpha &= \frac{M_p}{M_*} \frac{a}{D} \\ &= 0.3 \left(\frac{M_p}{M_{\oplus}} \right) \left(\frac{a}{1\text{AU}} \right) \left(\frac{M_*}{M_{\odot}} \right)^{-1} \left(\frac{D}{10\text{pc}} \right)^{-1} \mu\text{as}, \end{aligned} \quad (1)$$

where M_p denotes the planetary mass, M_* is the stellar mass, a represents the semi-major axis of the planet,

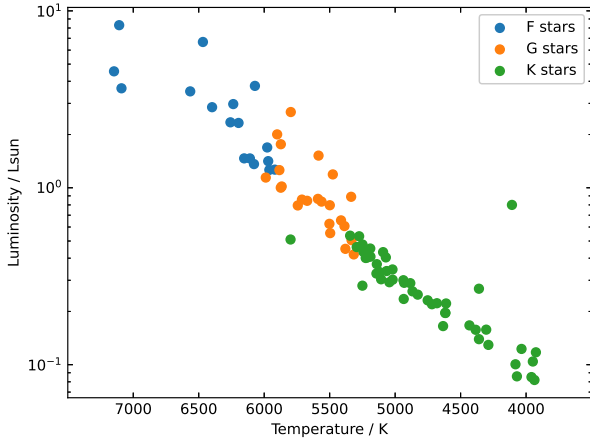


Figure 1. The Hertzsprung-Russell diagram depicts CHES targets, comprising 19 F stars, 24 G stars, and 51 K stars.

and D is the stellar distance to the solar system. Consequently, the astrometric signal induced by an Earth-mass planet at 1 au, causing a solar-mass star to wobble 10 pc away, is measured at $0.3 \mu\text{as}$ as aforementioned.

3. STELLAR ACTIVITY MODEL

We formulated a model to simulate the emergence of spots and faculae on solar-type stars. Subsequently, we generated synthetic observational data, encompassing both photometry and astrometry, spanning a five-year duration to match the expected time baseline of CHES.

3.1. Analytic centroid approximation

The difference in intensity of stellar magnetic features, including spots and faculae, compared to the photosphere, leads to variations in the stellar photocenter as the star rotates and features evolve. To evaluate the influence of jitters on the detection of terrestrial planets, we constructed a model employing `butterpy` (Claytor et al. 2022) to simulate the presence of spots and faculae. Subsequently, we computed the astrometric time-series.

We considered a star with a radius R_* and defined Cartesian coordinates on the stellar surface to calculate variations in the photocenter across the stellar surface (Morris et al. 2018). The origin is placed at the center of the star, with the x-axis aligned along the stellar equatorial plane. The y-axis indicates the rotation axis, and the sign of the z-axis determines whether the feature is obstructed by the star. Thus, the position of the i th feature can be described as $\mathbf{r}_i = (x_i, y_i)$, where $r_i = |\mathbf{r}_i|$.

The total flux from the star is characterized by (Morris et al. 2018)

$$F_* = \int_0^{R_*} 2\pi I(r) dr, \quad (2)$$

where r is the distance to origin in unit of stellar radius, and $I(r)$ is limb-darkening law. We use a four-parameter the non-linear limb-darkening law introduced by Claret (2000),

$$\frac{I(\mu)}{I(1)} = \begin{cases} 1 - \sum_1^4 a_k (1 - \mu^{k/2}) & \mu > \mu_{cri} \\ 0 & \mu < \mu_{cri}, \end{cases} \quad (3)$$

where μ represents the position on the surface (cosine between the local surface and the line of sight), $\mu = \sqrt{1 - r^2}$, μ_{cri} is the drop-off point, a_k are limb-darkening coefficients, which are linked to stellar effective temperature and $\log g$ (Claret 2018).

We generated a bulk of spots and faculae in the stellar surface, and the flux contribution from each feature is determined by its position, area, and intensity. The intensity of the i th spot can be described as (Meunier et al. 2019):

$$F_{sp,i} = -C_{sp,i} A_i * \mu_i, \quad (4)$$

where $C_{sp,i}$ is the contrast of spot, A_i is the area of spot.

Here we assume that all features are circular, with a radius R_i , a position r_i and a true area A_0 . Features near limb will be foreshortened, approximated by an ellipse with a semi-major axis R_i and a semi-minor axis $R_i \sqrt{1 - r_i^2}$. Thus the projected area can be expressed as:

$$A_i = \sqrt{1 - r_i^2} A_0. \quad (5)$$

The projected area is independent of R_i , so we only concern on true area and position of spots or faculae.

In this study, the temperature contrast C_{sp} is utilized. We assume that both the photosphere and the spot exhibit blackbody characteristics. Therefore, C_{sp} is described through the Planck function f (Meunier et al. 2019):

$$C_{sp} = 1 - \frac{f(T_{sp})I(\mu_i)}{f(T_{eff})I(\mu_i)}. \quad (6)$$

And the intensity of faculae is similar as spots:

$$F_{fa,i} = A_i C_{fa,i} * \mu_i. \quad (7)$$

The astrometric contribution in the x direction is the same for faculae and spots:

$$\begin{aligned} \Delta x &= \frac{R_*}{D} \sum \frac{F_i}{F_*} x_i \\ &= 0.465 \times 10^2 \left(\frac{R_*}{R_\odot} \right) \left(\frac{D}{10\text{pc}} \right)^{-1} \sum \frac{F_i}{F_*} x_i \quad \mu\text{as}, \end{aligned} \quad (8)$$

the formula in y direction is similar.

3.2. Fundamental stellar parameters

In our model, the astrometric precision is directly influenced by the stellar radius in Equation 8, while the planetary signal is connected to the stellar mass in Equation 1. In addition to mass and radius, the activity level of star determines numbers and distribution of magnetic features. In this paper, we adopt the dimensionless parameter activity level defined by Aigrain et al. (2015), with the assumption that the Sun’s level is 1. This parameter will be discussed further in section 3.3.

Subsequently, our objective is to determine temporal variations in stellar activity, encompassing both the rotation period and cycle period. Rotation is a common observation in many stars, with typical periods ranging from a few days to a few hundred days. Due to the planned uneven sampling strategy during CHES observations (Ji et al. 2022), the shortest cadence is about two or three days, and short-term rotation also impacts astrometry. The rotation rate of each target is yet to be determined for simulating. Previous studies have deduced stellar rotation periods from lightcurves or spectral observations (McQuillan et al. 2014; Pan et al. 2020; Jin et al. 2023), revealing a correlation between rotation period and characteristics in large star samples from TESS or Kepler (Witzke et al. 2020; Reinhold & Hekker 2020).

We have chosen to utilize the empirical law that establishes a relationship between the Rossby number R_o and the estimated turnover timescale τ_c with the rotation period. The rotation period can be estimated according to Noyes et al. (1984):

$$P_{rot} = R_o \times \tau_c, \quad (9)$$

where the Rossby number is estimated by $\log R'_{HK}$ (Mamajek & Hillenbrand 2008), and the turnover timescale is linked to B-V (Suárez Mascareño et al. 2016). Figure 2 presents the theoretical and observed rotation period of 33 stars in our samples. The observed periods closely align with theoretical values, falling within the margin of error for roughly 80% of the stars. Despite the more substantial disparity between the two stars with the shortest periods, our attention is directed towards stars characterized by moderate periods. This arises from the fact that only approximately 10% of FGK stars manifest rotation periods of less than five days in the Kepler and K2 samples (McQuillan et al. 2014; Reinhold & Hekker 2020). Consequently, we derived rotation periods for stars lacking observed periods with Equation 9.

Stellar activity cycles are widely hypothesized to arise from dynamo processes. The solar cycle spans approximately 11 years, and there is evidence suggesting a correlation between activity cycle periods and rotation pe-

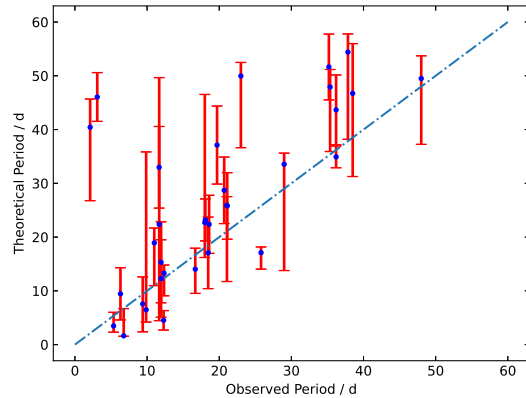


Figure 2. Theoretical and observed rotation periods of 33 stars in our sample, the dashed line denotes the observed periods equal to theoretical periods. Errorbars indicates the period ranges from uncertainties of $\log R'_{HK}$.

riods (Noyes et al. 1984; Brandenburg et al. 1998). In our study, we employed a relationship tailored for FGK stars to estimate the cycle period (Irving et al. 2023). The cycle period and rotation period details are presented in the appendix. All target cycle periods are shorter than five years (the time baseline of CHES), enabling us to assume that the maximum stellar activity jitter in a cycle is estimated in our simulations.

3.3. Determination of activity level

Given that the activity level serves as an adjustable scale factor governing the average rate of spot and facula emergence (Aigrain et al. 2015), it becomes imperative to ascertain the activity level for each target. We determine the activity level using the chromospheric index $\log R'_{HK}$ and photometric variability as detailed below.

Initially we derived the lightcurves of 78 stars observed by TESS by the package `lightkurve` (Lightkurve Collaboration et al. 2018), encompassing the simple aperture photometry (SAP Flux) and the presearch data conditioning SAP flux (PDCSAP Flux). For both of type data, we removed outlier and bad data based on quality flag of TESS. Each light curve was scrutinized visually to avoid systematic errors. And the SAP Flux is preferred as the long-term trends are removed in PDCSAP Flux. Subsequently, the peak-to-peak amplitude values were derived to characterize variability of each lightcurve (Hojjatpanah et al. 2020). Given that the timescale of a single sector is much shorter than the stellar cycle period, for stars observed in two or more sectors, we individually processed each light curve and calculated the peak-to-peak values. In most cases, the differences in peak-to-peak values between different sec-

tors are quite small, and the mean peak-to-peak values are derived as input parameters in our model. For individual stars, we found that the peak-to-peak value from one sector is significantly higher than the others, and no systematic errors were found. In this case, the lightcurve of this sector is considered to have been observed observed during the more active phase of the star, and the mean value of PDCSAP Flux and SAP Flux of was used. Additionally, we calculated the variations of Sun from 25 Feb. 2003 to 25 Feb. 2020 as a comparison.

We identified a quadratic relation between peak-to-peak values and $\log R'_{HK}$, which represents the contribution of the CaII H and K lines to the bolometric luminosity of the star (Noyes et al. 1984). This index can be derived through spectral observations, such as those obtained by instruments like LAMOST (Zong et al. 2018). Figure 3 displays $\log R'_{HK}$ and peak-to-peak variability of 78 samples and Sun (left panel). The variation of the Sun was calculated based on Total Solar Irradiance(TSI) data ¹. Photometric variations were utilized to relate $\log R'_{HK}$ activity level in our model. We established a grid of levels from 0.5 to 5, and generated 100 simulated lightcurves at each level. Figure 4 reveals a parabolic relationship between activity level and peak-to-peak variation, consistent with the results of Aigrain et al. (2015). Consequently, activity levels of targets with observed lightcurves could be determined.

For stars not observed by TESS or Kepler, we fitted the relationship of activity levels and $\log R'_{HK}$ to ascertain their activity levels. Figure 3 depicts relationship between $\log R'_{HK}$ and activity level (right panel). We found there is a quadratic relation between activity level and $\log R'_{HK}$ in our samples and the Sun, and the relations for stars of different spectral types (FGK) are consistent. Notably, the star with the highest activity level is HD 17925, an RS CVn Variable star considered an outlier and excluded during the fitting process. We infer that this relation is applicable to other solar-type stars as well.

3.4. Simulated spots and faculae

The primary parameter categories of spots and faculae include distribution, variability, contrast and size. We utilize the Python package `butterpy` to generate spots with spatial and temporal distribution (Claytor et al. 2022).

Over the approximately 11-year solar activity cycle, spots emerge within active regions at high latitudes initially. Subsequently, these regions migrates toward the

equator, indicating some overlap between consecutive cycles, resulting in a butterfly diagram illustrating the latitude distribution of spots over time. In our model, we set the overlap duration to be 10% of cycle period. The butterfly diagram has also been observed in other stars (Bazot et al. 2018; Nielsen et al. 2019). In our model, we apply the butterfly spot emergence feature of `butterpy`. Because the faculae typically existed around spots, we add a facula near each spot in our model (Borgniet et al. 2015). The input parameters needed for `butterpy` are given in Table 1. Active regions are positioned at medium latitudes in our samples. Since polar spots have been observed in several fast rotators using Doppler and Zeeman Doppler imaging (Vogt & Penrod 1983; Strassmeier 2009), we also generated spots and faculae at latitudes ranging from 55° to 85° for samples with periods shorter than five days. We found that the difference in standard deviations of astrometric jitters between these two models (i.e., medium latitudes and high latitudes) is approximately 0.1 μ as. The latitudes of the activity regions are considered less influential due to the symmetry of our model.

We estimated the temperature difference between the photosphere T_* and spots T_{sp} of FGK stars (Berdyugina 2005; Namekata et al. 2019), revealing a trend with effective temperature T_* of the star:

$$\begin{aligned} \Delta T &= T_* - T_{sp} \\ &= 3.58 \times 10^{-5} T_* + 0.249 T_* - 808 \quad (\text{K}). \end{aligned} \quad (10)$$

As the area ratio between penumbral and umbral of sunspots is approximately 4 to 5 (Solanki 2003), the penumbral is significantly hotter than the umbra ($\sim 1000\text{K}$) (Johnson et al. 2021). Therefore, we weigh the differential temperature based on the relative areas in the penumbrae and umbrae within the range 0.2 and 0.6. The coefficient used is similar to that employed by Lagrange et al. (2010). The contrasts of stellar faculae are poorly constrained, we use an intensity contrast in the optical band for G-type stars (Borgniet et al. 2015):

$$C_{fa} = 0.131618 - 0.218744\mu + 0.104757\mu^2, \quad (11)$$

the simulated spectra show that the differences in facular contrasts between K-type and G-type stars are relatively small at the band of CHES, and the contrasts of F-type stars are slightly lower than GK stars (Norris 2019; Norris et al. 2023). The contrasts of faculae are much lower than those of spots and are observed generated near spots. However their area is greater as observed on the Sun, the contribution from faculae is therefore expected to be significant. In this paper we use the area ratio to describe the size of faculae because

¹ TSI data is from observation of The Solar Radiation and Climate Experiment (SORCE)

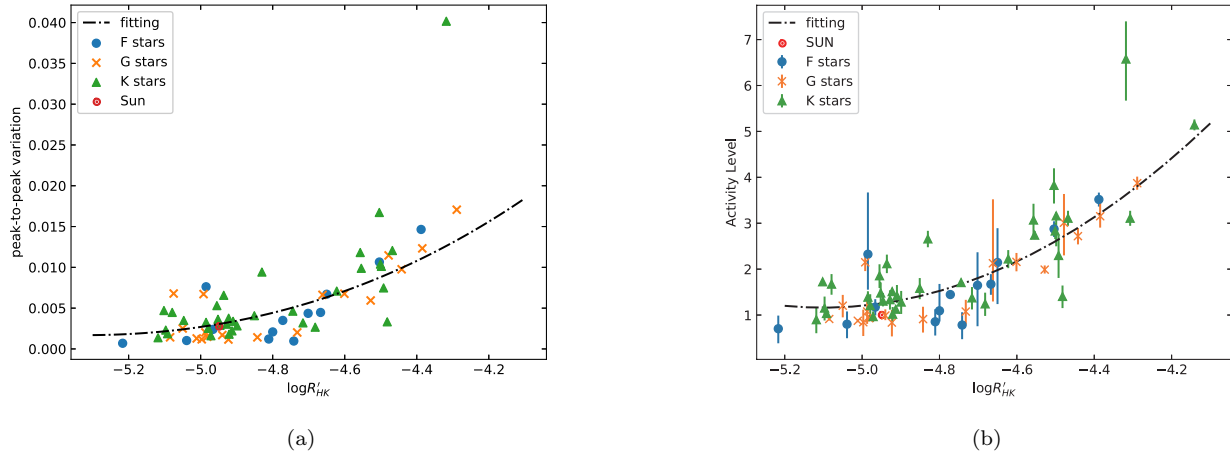


Figure 3. *Left panel:* the relation between $\log R'_{HK}$ and peak-to-peak variations of photometry, the dashed line shows a parabolic fitting. *Right panel:* same for the relation between $\log R'_{HK}$ and activity level, while errorbars shows the uncertainties of activity level. The blue circle, orange cross, and green triangle correspond to F,G,K stars respectively.

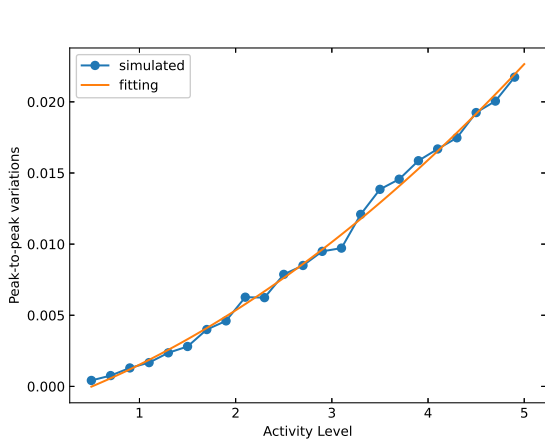


Figure 4. The activity level with photometric peak-to-peak variations. The step of activity level is 0.2, the y-coordinate of each point indicates the mean peak-to-peak variations of 100 simulated lightcurves.

we add a facula near each spot (Borgniet et al. 2015), the overlap situation was not considered in our simulations, given that the areas of features are significantly smaller compared to the stellar disk. We employed a lognormal distribution for spots in our simulations (Bogdan et al. 1988; Solanki & Unruh 2004; Baumann & Solanki 2005). Additionally, we used a lognormal distribution to describe the ratio between faculae and spots (Borgniet et al. 2015).

Given that the emergence of spots and facula occurs within a few hours (Howard 1992), smaller than our time step, and we focus here on planets with periods of a few hundred days, we neglected the growing process and assumed that all features are created with maximum

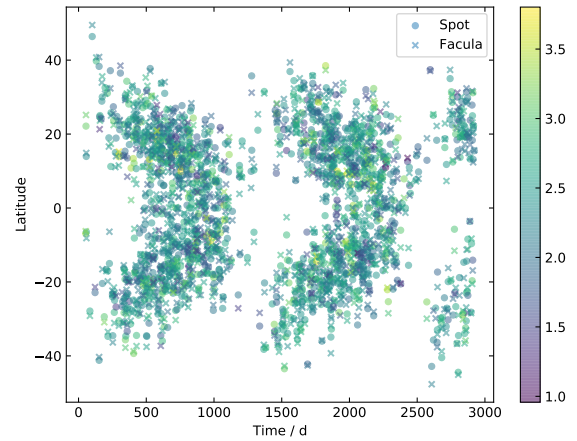


Figure 5. An example of the temporal and spatial evolution of spots and faculae on the surface of target 107 Psc, with a cycle period about 1200 days. Stellar magnetic features latitude distribution follows the butterfly diagram during eight years, the circles represent spot, and the crosses represent facula. The colorbar shows logarithmic areas of features, in unit of MSH (millionths of solar hemisphere).

area (Borgniet et al. 2015). We employed a parabolic decay law for both spots and faculae (Gilbertson et al. 2020).

All input parameters of spots and faculae for our model are summarized in Table 1. For each star, the simulations last for eight years with a 0.9 day time step (total 3000 points) to ensure the simulation covers the entire cycle. At the beginning of each simulation no features are present on the stellar surface. Thus, we extracted the middle five years, assuming the simulation has reached a steady state. Figure 5 displays an exam-

Table 1. Input parameters for spots and faculae

Category	Parameter	Value/range	Unit	Reference
Stellar activity	Cycle Period	0-60	yr	
	Cycle Amplitude	0.1-5	-	
	Cycle Overlap	0.1	-	Aigrain et al. (2015)
Spots properties	Mean initial size	46.5	MSH ^a	
	Standard size deviation	2.14	MSH	
	Max size	1500	MSH	Meunier et al. (2019)
	Decay rate	43.9	MSH/d	
	Max ave latitude	35	deg	
	Min ave latitude	7	deg	Claytor et al. (2022)
Faculae properties	log Mean size ratio	0.8	-	
	log Standard size ratio	0.4	-	
	Latitude deviation	3	deg	
	Longitude deviation	3	deg	
	Decay rate	21.9	MSH/d	Borgniet et al. (2015)

NOTE—a: micro stellar hemispheres

ple pattern of 107 Psc to show stellar magnetic features latitude distribution over eight years.

4. DETECTION EFFICIENCIES

Moreover, we used the inject-recover method to estimate detection limits of each star. We randomly generated 5000 planets in the parameters space. Since the main goal of CHES is to search Earth-like planets, we set the planetary mass range to of 0.5 to 5 Earth masses. All planets were placed in the habitable zone, with the inner and outer semi-major axis boundaries calculated based on the Runaway Greenhouse limit and Maximum Greenhouse limit, respectively (Kopparapu et al. 2014). All orbital elements and planetary masses followed a uniform distribution. The stellar wobbles due to a planet represent Keplerian orbit motion and can be derived through the Thiele-Innes equations (Thiele 1883). Apart from the photocenter shifts due to stellar activity, we also account for other measurement errors, including photon noise, telescope error, and calibration errors. Gaussian noise, with a mean of 0 and standard deviations of $0.7 \mu\text{as}$ is added in the simulations (Ji et al. 2022).

For planets retrieval, the Lomb-Scargle periodograms are utilized (Horne & Baliunas 1986). The period with the highest power is considered as a prior during fitting. Then we use a sinusoidal function based on the Thiele-Innes equations to fit planetary signal (Jin et al. 2022). In the fitting process, we assume all planets are in circular orbits to reduce computation. The amplitude of the sinusoidal function is denoted as α , and the planetary mass is derived using Equation 1. We con-

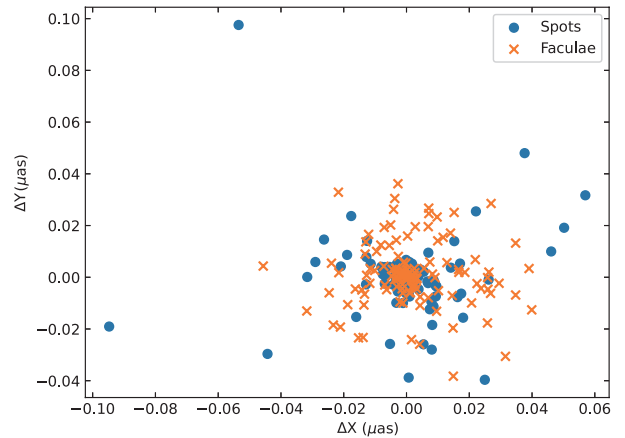


Figure 6. The photocenter jitter due to spots and faculae of HD 103095 during five years, the blue circles and orange crosses represent effects of spots and faculae, respectively.

sider a planet to be recovered if both the derived period and mass within 30% error is recovered. Additionally, we use the SNR criteria as a comparison. The SNR in astrometric planets is defined as (Unwin et al. 2008):

$$\text{SNR} = \frac{\alpha}{\sigma} N_{vis}^{1/2}, \quad (12)$$

where the σ is the standard deviations of total noise, N_{vis} is the number of observation, depending on observational strategy of CHES (Tan et al., in prep.). Table 2 further presents DHZ (the distance to the center of habitable zone) for each target.

5. RESULTS OF JITTER AMPLITUDE AND DETECTION EFFICIENCY

We applied the methods outlined in Section 3 to 94 stars. First we found there is a quadratic relation between activity level and the photometric peak-to-peak variations, as expected by Aigrain et al. (2015). We then fitted a parabolic relation to calculate activity levels from $\log R'_{HK}$ for our samples, and as the Sun corresponds to this relation as well, we infer that the relation can be extended to other FGK stars. Subsequently, we generated astrometric timeseries due to spots and faculae for each target. As an example, we consider the target HD 103095, a K-type star with no detected planets. The astrometric jitters of its photocenter are shown in Figure 6, with an amplitude about $0.1 \mu\text{as}$, which is lower than signal from an Earth-mass planet ($\sim 0.3 \mu\text{as}$). We derived the standard derivations in two directions of all targets, as shown in Figure 7. It was found that for more than 95% of the targets, the standard deviations of photocenter shifts due to activity are less than $1 \mu\text{as}$. Figure 8 shows the mean shifts of photocenter in our samples, which are within $0.4 \mu\text{as}$ for all stars. And the errorbars represents amplitudes of jitters. We found several stars with amplitudes larger than $1 \mu\text{as}$, because of shorter distance (e.g. Alpha Cen A and eps Eri) or the combination of higher activity level, larger size and short distance (e.g. eta Cas A). We found the jitter in the Y direction is slightly smaller than that in the X direction because of the symmetry of butterfly diagram. And we derived the detection rates corresponding to terrestrial planets in habitable zone. The results for all targets are provided in Table 2. The inject-recover results of 107 Psc is shown in Figure 9. We found about 95% planets with $\text{SNR} > 6$ were recovered, consistent with those of Perryman et al. (2014).

The histogram of detection efficiency is shown in the left panel of Figure 10, with nearly 95% stars having a detection rate above 80%. The detection efficiency decreases for some cold stars, such as HD 32450 and HD 21531, due to the weak planetary signal from a closer habitable zone. Despite several stars, such as α Cen A and eps Eri having an obvious jitter, their detection efficiencies remain high because the planetary signals also increase as the distance gets closer. The right panel of Figure 10 displays the detection efficiencies versus the distance of the stars. In our sample, six stars have detection efficiencies below 80%; five of them are located 8 pc away, exhibiting a slightly weak planetary signal. Notably, the subgiant alf CMi has a detection efficiency of about 79.8% due to its much more distant habitable zone. The period corresponding to habitable planets around alf CMi is approximately the same length

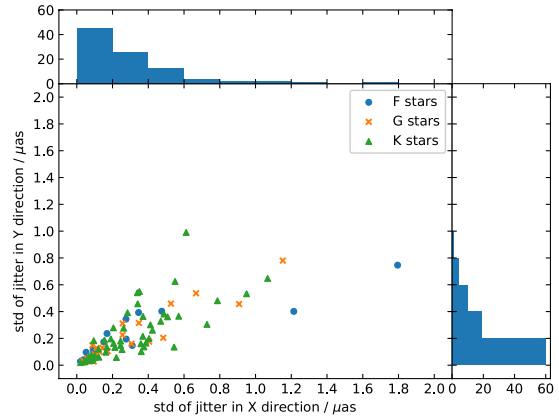


Figure 7. The standard deviations of astrometric jitter in two directions of all targets from simulations. The blue circle, orange cross, and green triangle correspond to F,G,K stars respectively. The two histograms shows jitter’s distribution in our samples.

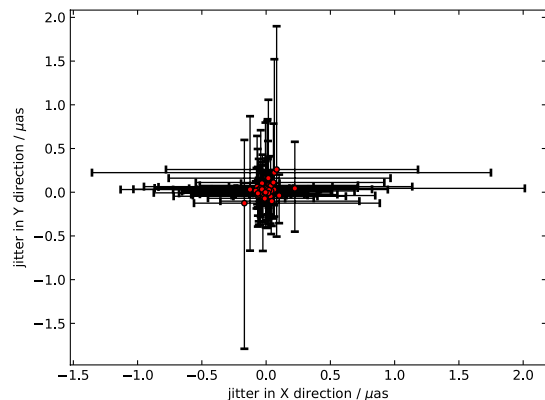


Figure 8. The mean jitter caused by stellar spots and faculae from simulations. The errorbars indicate the maximum and minimum jitter duration five years.

as the time baseline of CHES, making planet characterization difficult.

6. CONCLUSIONS AND DISCUSSIONS

In this study, we conducted simulations to evaluate the influence of stellar activity on the detection of terrestrial planets in the context of the ultra-high precision astrometry space mission, CHES, which aims to perform measurements on approximately 100 nearby stars. Our model, implemented within `butterpy`, generated simulated astrometry data for the identified CHES targets. We estimated the contrast of spots based on Equation

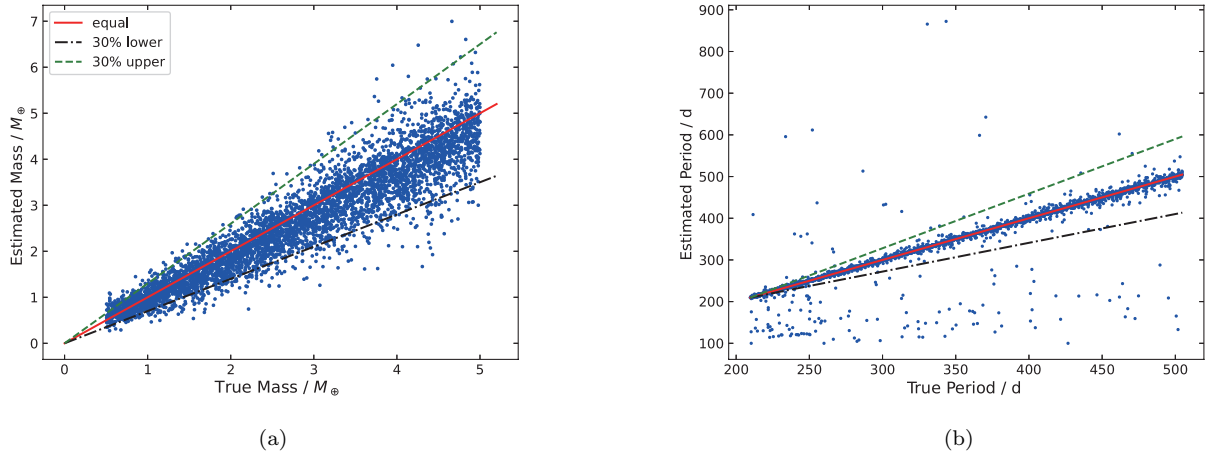


Figure 9. Properties of fitted mass (*left panel*) and periods (*right panel*) vs. true values of 107 Psc, every points indicates a injected planet. The red solid line indicates equal values, and the green dashed line and the black dashdotted indicates a 30% upper and lower uncertainty level, respectively.

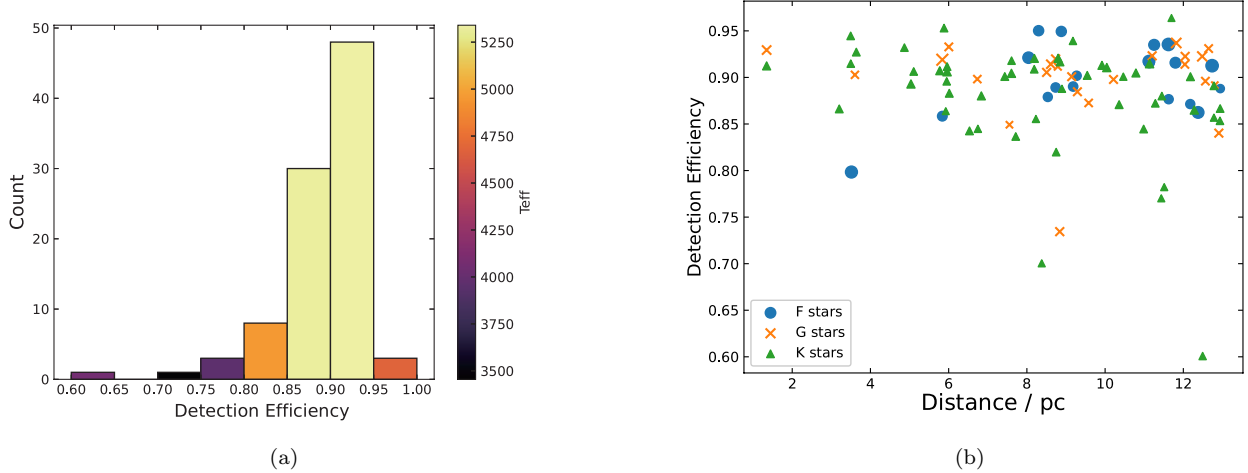


Figure 10. *Left:* The histogram of detection efficiency, the colorbar show mean effective temperature in each bin. *Right:* The detection efficiency and distance of all targets, sizes of each point indicate stellar radius. The blue circle, orange cross, and green triangle correspond to F,G,K stars respectively.

10, which applies to stars with effective temperatures between 3000 to 7000 K (Berdyugina 2005; Namekata et al. 2019). Notably, there are about a dozen stars beyond this temperature range. As the empirical formula is believed to overestimate contrasts, especially for hotter stars (Borgniet et al. 2015; Meunier et al. 2019). Borgniet et al. (2015) also estimated a lower bound of spots contrasts. In this paper, we choose Equation 10 as an extreme case because higher contrasts cause larger astrometric noise. Similarly, the facular effect of F-type stars can also be overestimated in our simulation as in-

troduced in Section 3.4. Therefore, higher detection efficiency of CHES is actually possible.

As some peak-to-peak values were derived from multiple sectors, there are errors in each star’s activity level, as depicted in Figure 3. The astrometric jitters of ten targets with larger errorbars were calculated based on their maximum activity level value. Tet Per exhibits a noise about $1.3 \mu\text{as}$ with an activity level of approximately 2.5. While noise from stellar activity is still not the dominant factor for other stars, with standard deviations lower than $0.7 \mu\text{as}$. These ten stars are indicated in Table 2.

The determination of each star’s activity level relied on the chromospheric index $\log R'_{HK}$. Our observations revealed a discernible correlation between increased activity levels and heightened variability in both photometry and astrometry, best described by a parabolic relation. Subsequent analysis of the time series facilitated the estimation of detection efficiencies for planets within the habitable zone of each target. Notably, the influence of stellar activity on astrometry was found to be minimal, with photocenter jitter measuring less than $1 \mu\text{as}$ for around 95% of the targets. In the context of terrestrial planet detection, the astrometric method demonstrated superior efficacy compared to current radial velocity and transit methods.

We compared our findings with the results of Meunier & Lagrange (2022), who estimated the astrometric noise from stellar activity of Theia’s targets. Among the 37 common targets, the differences in astrometric jitter are less than $0.3 \mu\text{as}$ for approximately 80% of the stars.

In this work, we intentionally exclude the consideration of other stellar characteristics, such as oscillation, granulation, and supergranulation, as their expected impact on astrometry is deemed negligible (Sowmya et al. 2021). The associated timescales (Staude et al. 1999; Borgniet et al. 2015; Chiavassa et al. 2017) are considerably shorter than the observation cadence of the Closeby Habitable Exoplanet Survey (Ji et al. 2022). Our focus remains on single-planet systems, although multi-planet systems are prevalent in observational datasets. Approximately 10 targets in our sample are identified as hosting hot Jupiters or Neptunes based on radial velocity measurements. The presence of existing gas-giants may obscure signals from Earth-like planets, a factor we plan to address in forthcoming study.

In our simulations, stellar inclinations are consistently set in an edge-on configuration. While Meunier et al. (2019) concluded that the amplitude of radial velocity reaches a maximum in this configuration, Sowmya et al. (2021) found that the largest astrometric jitter occurs at intermediate inclinations. A nuanced exploration of the impact of inclinations is scheduled for future investigations. In this work, we do not consider the growth phase

of activity regions, which is not well understood observationally at present. Since the growth rates of sunspots are much faster than their decay rates (Howard 1992; Forgács-Dajka et al. 2021), and nearly 90% of the targets in our sample exhibit higher activity levels than the Sun, we chose to disregard this effect in our study. The total flux contribution, including the growth process, is estimated to be less than 1.0% based on simulations by Aigrain et al. (2015). Assuming that the dip in flux originates from only one spot on the edge, the photocenter shifts are approximately $0.4 \mu\text{as}$ for a solar-like star at a distance of 10 pc, which is comparable to the results obtained from our no-growth model. Given the limited understanding of spot evolution, this growth phase will be incorporated in future study to provide a more comprehensive description of the astrometric noise from stellar activity at small timescales. This approach aims to contribute to a more holistic understanding of the challenges and opportunities associated with astrometric detection methods, especially when considering diverse planetary systems. Furthermore, our forthcoming research will systematically investigate additional factors influencing the astrometric precision of CHES, including comprehensive considerations such as the potential presence of planets around the reference stars and the stability of the satellite.

ACKNOWLEDGEMENTS

- 1 We thank the referee for constructive comments and sug-
- 2 gestions to improve the manuscript. This work is finan-
- 3 cially supported by the National Natural Science Foun-
- 4 dation of China (grant Nos. 12033010 and 11773081),
- 5 the Strategic Priority Research Program on Space Sci-
- 6 ence of the Chinese Academy of Sciences (Grant No.
- 7 XDA 15020800), and the Foundation of Minor Planets
- 8 of the Purple Mountain Observatory.

Software: astropy (Astropy Collaboration et al. 2013), butterpy (Claytor et al. 2022), lightkurve (Lightkurve Collaboration et al. 2018), matplotlib (Hunter 2007), PyMsOfa (Ji et al. 2023), scipy (Virtanen et al. 2020)

APPENDIX

Table 2. The parameters of target stars for CHES mission

identifier	Level	T_{eff} (K)	$\log g$	radius (R_{\odot})	mass (M_{\odot})	D (pc)	TS	$\log R'_{HK}$	P_{rot} (d)	P_{cyc} (d)	DHZ (au)	$\sigma(\Delta x)$ (μas)	$\sigma(\Delta y)$ (μas)	efficiency
107 Psc	1.03	5190	4.54	0.83	0.88	7.61	K1V	-5.00(23)	51.6	1241.1	0.93	0.059	0.029	0.904
11 Lmi(*)	2.13	5499	4.43	0.98	0.96	11.20	G8V	-4.66(23)	22.4	1144.1	1.20	0.22	0.158	0.923
12 Oph	1.78	5293	4.58	0.81	0.91	9.92	K0V	-4.72(15)	25.9	1161.0	0.93	0.089	0.127	0.913
36 Oph A	1.80	5121	4.52(6)	0.89(6)	0.96(6)	5.96	K2V	-4.74(23)	28.7	1302.8	0.80	0.385	0.18	0.906
36 Oph B	1.95	5143	4.66	0.72	0.87	5.96	K1V	-4.66(3)	25.8	1311.2	0.79	0.288	0.16	0.912
41 Ara A(*)	1.16	5380	4.63	0.77	0.93	8.79	G9V	-4.94(23)	48.4	1188.3	0.91	0.07	0.057	0.912
54 Psc	1.17	5275	4.51	0.87	0.90	11.14	K0.5V	-5.05(15)	49.5	1260.8	1.00	0.058	0.044	0.915
61 Cyg A	1.42	4305	4.56	0.71	0.67	3.49	K5V	-4.91(15)	47.9	1489.6	0.58	0.069	0.161	0.945
61 Cyg B	1.86	3948	4.55	0.69	0.61	3.50	K7V	-4.96(15)	54.4	1571.7	0.48	0.327	0.241	0.915
61 UMa	1.99	5502	4.55	0.87	0.97	9.58	G8V	-4.53(15)	14.0	1084.5	1.06	0.101	0.082	0.873
61 Vir	0.87	5562	4.44	0.98	0.98	8.51	G7V	-5.01(15)	33.6	897.2	1.22	0.05	0.045	0.905
70 Oph B	1.65	4360(27)	4.57(27)	0.71(27)	0.70(27)	5.11	K4V	-4.76(3)	37.1	1517.8	0.75	0.364	0.215	0.906
85 Peg	0.91	5336	4.45(34)	0.91(37)	0.89(37)	12.65	G5V	-4.84(23)	23.2	807.8	1.28	0.041	0.018	0.931
alf Cen A	1.19	5585(11)	4.31(31)	1.11(30)	1.13(30)	1.35	G2V	-5.01(9)	34.9	926.2	1.64	0.332	0.202	0.929
alf Cen B	1.31	5151(30)	4.38(30)	0.81(30)	0.86(30)	1.35	K1V	-4.92(5)	43.7	1335.9	0.94	0.048	0.037	0.912
alf CMi	1.50	6775(30)	3.74(30)	1.82(30)	1.53(30)	3.51	F5IV	-4.82(3)	2.9	106.0	3.22	0.056	0.033	0.798
alf Men	1.35	5590(30)	4.20(30)	0.95(30)	0.98(30)	10.21	G7V	-4.89(15)	29.8	951.79	1.24	0.015	0.017	0.898
bet Com	1.45	5969	4.39	1.11	1.10	9.18	F9.5V	-4.77(30)	13.3	525.3	1.54	0.124	0.088	0.890
bet CVn	0.93	5884	4.40	1.08	1.07	8.61	G0V	-4.98(30)	21.1	586.4	1.46	0.143	0.155	0.914
bet Hyi	1.20	5901(30)	4.14(19)	1.76(19)	1.12(19)	5.84	G0V	-5.05(30)	24.4	618.46	2.15	0.086	0.106	0.919
bet TrA	1.55	7108	4.22(6)	1.73(27)	1.58(27)	12.38	F1V	-4.80(1)	5.3	199.3	1.60	0.034	0.024	0.862
bet Vir	1.24	6071	4.00	1.75	1.13	11.12	F9V	-4.96(15)	13.7	390.0	2.49	0.191	0.188	0.917
chi Dra	1.09	6119	4.28(16)	1.31	1.20(27)	8.30	F7V	-4.80(1)	15.4	581.4	1.89	0.114	0.114	0.950
chi01 Ori	3.15	5988	4.49	0.99	1.10	8.84	G0V	-4.38(23)	3.5	587.1	1.38	0.285	0.157	0.734
e Eri	0.84	5413	4.48	0.92	0.94	6.00	G6V	-5.00(15)	34.1	928.6	1.09	0.306	0.27	0.933
eps Eri	2.2	5065	4.61	0.76	0.85	3.20	K2V	-4.6(15)	22.4	1366.8	0.81	1.223	1.305	0.866
eps Ind	1.58	4611	4.57	0.74	0.73	3.64	K5V	-4.85(15)	42.0	1441.1	0.67	0.645	0.147	0.927

Table 2 continued

Table 2 (continued)

identifier	Level	T_{eff} (K)	logg	radius (R_{\odot})	mass (M_{\odot})	D (pc)	TS	$\log R'_{HK}$	P_{rot} (d)	P_{cyc} (d)	DHZ (au)	$\sigma(\Delta x)$ (μas)	$\sigma(\Delta y)$ (μas)	efficiency
eta Cas A(*)	2.32	5919	4.41(34)	1.19(37)	1.03(37)	5.84	F9V	-4.99(3)	17.5	484.6	1.46	0.251	0.212	0.864
eta Cas B	2.12	3973(37)	4.56(37)	0.60(37)	0.60(37)	5.93	K7Ve	-4.94(3)	53.3	1590.2	0.42	0.069	0.033	0.858
gam Lep	1.17	6258	4.29	1.30	1.22	8.88	F6V	-4.97(15)	6.6	187.2	1.94	0.44	0.235	0.949
gam Pav	0.85	6109	4.43	1.08	1.15	9.27	F9V	-4.81(15)	5.7	210.9	1.55	0.273	0.163	0.902
gam Ser	0.78	6236	4.18	1.48	1.21	11.25	F6IV	-4.74(23)	6.1	256.0	2.19	0.109	0.071	0.935
gam Vir A	0.80	7147	4.04(24)	1.95(6)	1.39(35)	11.62	F1-F2V	-5.04(15)	12.2	313.1	2.56	0.056	0.024	0.935
gam Vir B	3.74	7090(8)	4.49(8)	1.95(35)	1.37(35)	12.74	F0mF2V	-4.30(23)	1.5	355.7	2.30	0.227	0.341	0.913
i Boo A	2.22	5820(33)	4.33(32)	0.87(33)	0.97(33)	12.94	F5V	-4.59(23)	12.3	761.3	1.33	0.106	0.063	0.888
i Boo B	1.55	5820(33)	4.11(6)	0.66(33)	0.55(33)	12.81	G9	-4.80(10)	24.7	930.2	1.33	1.04	0.87	0.892
iot Peg	1.67	6565	4.25	1.45	1.36	11.80	F5V	-4.67(23)	2.4	122.3	2.32	0.117	0.05	0.916
kap01 Cet	2.93	5712	4.50	0.95	1.02	9.15	G5V	-4.39(15)	7.6	835.4	1.22	0.049	0.026	0.901
ksi Boo A	2.72	5496	4.53	0.86	0.90	6.73	G7Ve	-4.44(3)	9.4	1076.5	1.00	0.087	0.077	0.898
ksi Boo B	3.04	4288	4.64	0.65	0.67	6.75	K5Ve	-4.42(1)	12.3	1610.8	0.53	0.382	0.33	0.845
ksi UMa A	3.85	5977(34)	4.19(23)	1.10	1.15(21)	8.73	F8.5	-4.28(23)	1.7	446.3	1.68	0.028	0.016	0.889
ksi UMa B	3.87	5476(34)	5.04(34)	1.00(37)	0.96(29)	8.73	G2V	-4.29(23)	3.3	821.8	1.47	0.054	0.045	0.923
lam Aur	0.91	5873	4.25	1.28	1.06	12.48	G1.5IV	-5.09(34)	26.9	651.8	1.73	0.163	0.215	0.923
lam Ser	0.84	5901	4.20	1.35	1.07	11.82	G0-V	-4.92(23)	17.1	1506.3	1.84	0.051	0.049	0.937
mu. Cas	2.15	5316	4.70(32)	0.68	0.72(17)	7.55	G5Vb	-4.99(3)	31.5	865.3	0.88	0.06	0.043	0.849
omi02 Eri	1.33	5092	4.51	0.85	0.85	5.04	K0V	-4.93(15)	40.4	1221.9	0.91	0.354	0.43	0.893
p Eri A	1.28	5020	4.58	0.78	0.83	8.19	K2V	-4.90(9)	40.8	1291.0	0.82	0.099	0.066	0.920
p Eri B	2.66	5107	4.68	0.70	0.86	8.19	K2V	-4.83(9)	37.8	1347.5	0.76	0.337	0.237	0.909
pi.03 Ori(*)	2.14	6398	4.05(18)	1.65(37)	1.25(37)	8.04	F6V	-4.65(7)	2.6	138.3	2.12	0.13	0.151	0.921
sig Dra	1.02	5242	4.59	0.80	0.90	5.77	K0V	-4.92(15)	37.2	1136.2	0.90	0.615	0.479	0.907
tau Cet	1.21	5333	4.56	0.83	0.92	3.60	G8V	-5.00(23)	35.3	957.2	0.97	0.311	0.235	0.903
tet Per(*)	1.65	6196	4.27	1.32	1.19	11.13	F8V	-4.70(15)	6.4	296.4	1.94	0.864	0.545	0.916
zet Dor	3.52	6153	4.45	1.07	1.17	11.63	F9VFe-0.5	-4.39(15)	2.2	367.9	1.55	0.355	0.342	0.877
zet TrA	2.87	6078	4.45	1.05	1.14	12.18	F9V	-4.50(23)	5.1	431.1	1.50	0.085	0.069	0.871
zet Tuc	0.70	5961	4.43	1.05	1.09	8.53	F9.5V	-5.22(15)	22.3	463.8	1.45	0.064	0.06	0.879
zet01 Ret	2.16	5744	4.54	0.90	1.03	12.04	G2.5	-4.60(15)	12.0	727.1	1.17	0.065	0.051	0.914
zet02 Ret	1.08	5866	4.48	0.98	1.06	12.05	G1V	-4.73(15)	13.1	566.8	1.32	0.498	0.217	0.923

Table 2 continued

Table 2 (continued)

identifier	Level	T_{eff} (K)	logg	radius (R_{\odot})	mass (M_{\odot})	D (pc)	TS	$\log R'_{HK}$	P_{rot} (d)	P_{cyc} (d)	DHZ (au)	$\sigma(\Delta x)$ (μas)	$\sigma(\Delta y)$ (μas)	efficiency
CD-57 1079	3.11	4186(18)	4.66	0.59	0.58	11.70	K7Vk	-4.47(23)	17.0	1700.6	1.32	0.097	0.095	0.964
HD 100623	1.13	5140	4.61	0.77	0.87	9.54	K0V	-4.91(15)	38.9	1203.9	0.84	0.108	0.031	0.902
HD 101581	1.71	4634	4.71	0.63	0.74	12.78	K4.5Vk	-4.74(15)	34.6	1459.9	0.58	0.176	0.14	0.857
HD 102365	0.99	5672	4.49	0.95	1.01	9.29	G2V	-4.94(15)	19.9	584.5	1.22	0.638	0.552	0.885
HD 103095	1.41	4934	4.70	0.66	0.81	9.18	K1V	-4.48(13)	6.7	628.4	0.68	0.303	0.087	0.939
HD 10780	1.72	5344	4.54	0.85	0.92	10.04	K0V	-4.70(23)	50.0	1232.1	0.99	0.98	4.62	0.911
HD 131977	1.38	4681	4.60	0.72	0.75	5.88	K4V	-4.88(23)	44.4	1461.1	0.67	0.421	0.244	0.953
HD 13445	1.37	5189	4.59	0.79	0.88	10.79	K1.5V	-4.76(23)	25.3	1135.7	0.88	0.361	0.81	0.905
HD 147513(*)	3.01	5873	4.49	0.97	1.06	12.91	G5V	-4.48(15)	7.2	685.4	1.30	0.605	0.297	0.840
HD 154363	1.66	4360	4.64	0.65	0.68	10.47	K4/5V	-4.76(23)	36.0	1451.2	0.54	0.289	0.273	0.901
HD 156384	1.88	4819	4.50(2)	0.80(36)	1.26(12)	6.84	K3V+K5V	-4.69(23)	30.7	1479.6	0.98	0.022	0.011	0.882
HD 157881	2.87	4035	4.53	0.72	0.63	7.71	K7V	-4.45(23)	15.3	1664.7	0.52	0.015	0.037	0.837
HD 17925(*)	6.58	5225	4.61	0.77	0.89	10.36	V-K1V	-4.32(15)	1.6	453.1	0.87	0.069	0.055	0.871
HD 191408	1.67	5044	4.23	0.76	0.78	6.02	K2.5V	-5.04(23)	52.6	1285.5	0.75	0.312	0.206	0.883
HD 192310	0.90	5071	4.54	0.82	0.85	8.80	K2+V	-5.12(23)	55.5	1302.0	0.88	0.161	0.125	0.921
HD 21531	3.27	4231(22)	4.67(22)	0.67(25)	0.66(37)	12.49	K5V	-4.38(23)	9.8	1728.5	0.43	0.13	0.082	0.601
HD 217357	2.83	4081	4.64	0.63	0.64	8.23	K7+Vk	-4.50(23)	19.5	1682.5	0.47	0.212	0.143	0.855
HD 219134	1.51	4884	4.59	0.75	0.80	6.53	K3V	-4.92(23)	46.1	1412.8	0.76	0.447	0.497	0.843
HD 222237	1.15	4752	4.62	0.71	0.76	11.45	K3+V	-5.10(15)	57.7	1369.7	0.68	0.722	1.017	0.880
HD 32147	0.97	4931	4.61	0.74	0.81	8.85	K3+V	-4.97(23)	50.2	1415.3	0.75	0.361	0.405	0.917
HD 32450	2.22	3455(26)	4.35(26)	0.62	0.61	8.38	K7V	-4.62(26)	29.4	1670.7	0.55	0.249	0.266	0.700
HD 36003	1.48	4616	4.62	0.69	0.73	12.94	K5V	-4.95(15)	49.9	1452.4	0.63	0.604	0.239	0.853
HD 37394(*)	3.07	5249	4.55	0.84	0.90	12.28	K1	-4.56(15)	18.9	1318.2	0.95	0.064	0.058	0.865
HD 38A(*)	2.30	3959	4.65	0.62	0.62	11.51	K6V	-4.49(23)	19.1	1703.0	0.43	0.062	0.033	0.782
HD 40307	1.15	4867	4.63	0.72	0.79	12.94	K2.5V	-5.16(15)	60.7	1332.6	0.72	0.283	0.195	0.867
HD 4628	1.21	4937	4.60	0.75	0.81	7.44	K2.5V	-4.98(15)	46.7	1307.7	0.77	0.168	0.149	0.901
HD 50281	2.74	4719	4.63	0.70	0.76	8.75	K3.5V	-4.55(15)	21.4	1505.7	0.67	0.049	0.041	0.820
HD 69830(*)	1.08	5387	4.50	0.89	0.93	12.56	G8:V	-4.99(15)	41.7	1153.3	1.06	0.326	0.191	0.896
HD 72673	1.30	5213	4.60	0.78	0.89	12.18	K1V	-4.95(15)	39.4	1157.3	0.87	0.428	0.189	0.901
HD 82106	3.16	4828	4.62	0.71	0.78	12.78	K3V	-4.50(23)	17.1	1490.9	0.70	0.063	0.049	0.891

Table 2 continued

Table 2 (continued)

identifier	Level	T_{eff} (K)	logg	radius (R_{\odot})	mass (M_{\odot})	D (pc)	TS	$\log R'_{HK}$	P_{rot} (d)	P_{cyc} (d)	DHZ (au)	$\sigma(\Delta x)$ (μas)	$\sigma(\Delta y)$ (μas)	efficiency
HD 85512	1.39	4433	4.60	0.69	0.69	11.28	K6Vk	-4.99(15)	52.9	1470.9	0.59	0.235	0.13	0.872
HD 88230	1.24	3893(20)	4.57	0.70	0.67	4.87	K6V	-4.47(23)	33.0	1603.4	0.51	0.164	0.081	0.932
LHS 2713	3.82	5019	4.63	0.73	0.83	10.99	K2V	-4.50(15)	17.1	1450.7	0.77	0.541	0.512	0.845
V AK Lep	1.98	5250	4.78	0.64	0.90	8.90	K3	-4.70(15)	27.3	1410.5	0.72	0.138	0.112	0.888
V TW PsA	3.11	4617	4.62	0.69	0.73	7.61	K4Ve	-4.31(15)	6.5	1674.1	0.63	0.03	0.035	0.918
V V2215 Oph	2.34	4385	4.60	0.69	0.69	5.95	K5V	-4.56(15)	22.7	1547.2	0.58	0.098	0.112	0.896
V V2689 Ori	5.14	3936	4.64	0.62	0.60	11.44	K6V	-4.14(23)	4.5	1819.8	0.43	0.03	0.011	0.770

NOTE—TS presents stellar spectral types, which are obtained from CDS. Level is the stellar activity introduced in Section 3.3. T_{eff} is the effective temperature of star. logg is the stellar surface gravity. D is the distance of stars. P_{rot} and P_{cyc} present the stellar rotation and cycle period, respectively. DHZ means the distance from the center of habitable zone. $\sigma(\Delta x)$ and $\sigma(\Delta y)$ present the standard deviations of astrometric jitter in X(Y) direction. efficiency is the detection efficiency of each star. The symbol * represents large range of activity level. The unmarked parameters, including T_{eff} , logg, radius and mass, are from Paegert et al. (2021). The rotation and cycle periods are from Sect. 3.2. References for other parameter are the following:(1) Noyes et al. (1984); (2) Perrin et al. (1988); (3) Duncan et al. (1991); (4) Baliunas et al. (1995); (5) Henry et al. (1996); (6) Allende Prieto & Lambert (1999); (7) Wright et al. (2004); (8) Luck & Heiter (2006); (9) Gray et al. (2006); (10) Mamajek & Hillenbrand (2008); (11) Holmberg et al. (2009); (12) Cvetkovic & Ninkovic (2010); (13) Isaacson & Fischer (2010); (14) Casagrande et al. (2011); (15) Pace (2013); (16) Carretta (2013); (17) Ramírez et al. (2013); (18) Paletou et al. (2015); (19) Jofré et al. (2015); (20) Terrien et al. (2015); (21) The Theia Collaboration et al. (2017); (22) Luck (2017); (23) Boro Saikia et al. (2018); (24) Aguilera-Gómez et al. (2018); (25) Houdebine et al. (2019); (26) Hojjatpanah et al. (2019); (27) Stassun et al. (2019); (28) Steinmetz et al. (2020); (29) Reiners & Zechmeister (2020); (30) Gomes da Silva et al. (2021); (31) Hirsch et al. (2021); (32) Perdigon et al. (2021); (33) Latković et al. (2021); (34) Soubiran et al. (2022); (35) Chulkov & Malkov (2022); (36) Yang et al. (2023); (37) Hardegree-Ullman et al. (2023);

REFERENCES

- Aguilera-Gómez, C., Ramírez, I., & Chanamé, J. 2018, *A&A*, 614, A55, doi: [10.1051/0004-6361/201732209](https://doi.org/10.1051/0004-6361/201732209)
- Aigrain, S., Llama, J., Ceillier, T., et al. 2015, *MNRAS*, 450, 3211, doi: [10.1093/mnras/stv853](https://doi.org/10.1093/mnras/stv853)
- Allende Prieto, C., & Lambert, D. L. 1999, *A&A*, 352, 555, doi: [10.48550/arXiv.astro-ph/9911002](https://doi.org/10.48550/arXiv.astro-ph/9911002)
- Astropy Collaboration, Robitaille, T. P., Tollerud, E. J., et al. 2013, *A&A*, 558, A33, doi: [10.1051/0004-6361/201322068](https://doi.org/10.1051/0004-6361/201322068)
- Baliunas, S. L., Donahue, R. A., Soon, W. H., et al. 1995, *ApJ*, 438, 269, doi: [10.1086/175072](https://doi.org/10.1086/175072)
- Baumann, I., & Solanki, S. K. 2005, *A&A*, 443, 1061, doi: [10.1051/0004-6361:20053415](https://doi.org/10.1051/0004-6361:20053415)
- Bazot, M., Nielsen, M. B., Mary, D., et al. 2018, *A&A*, 619, L9, doi: [10.1051/0004-6361/201834251](https://doi.org/10.1051/0004-6361/201834251)
- Berdugina, S. V. 2005, *Living Reviews in Solar Physics*, 2, 8, doi: [10.12942/lrsp-2005-8](https://doi.org/10.12942/lrsp-2005-8)
- Bogdan, T. J., Gilman, P. A., Lerche, I., & Howard, R. 1988, *ApJ*, 327, 451, doi: [10.1086/166206](https://doi.org/10.1086/166206)
- Borgniet, S., Meunier, N., & Lagrange, A. M. 2015, *A&A*, 581, A133, doi: [10.1051/0004-6361/201425007](https://doi.org/10.1051/0004-6361/201425007)
- Boro Saikia, S., Marvin, C. J., Jeffers, S. V., et al. 2018, *A&A*, 616, A108, doi: [10.1051/0004-6361/201629518](https://doi.org/10.1051/0004-6361/201629518)
- Brandenburg, A., Saar, S. H., & Turpin, C. R. 1998, *ApJL*, 498, L51, doi: [10.1086/311297](https://doi.org/10.1086/311297)
- Butler, R. P., Wright, J. T., Marcy, G. W., et al. 2006, *ApJ*, 646, 505, doi: [10.1086/504701](https://doi.org/10.1086/504701)
- Butler, R. P., Vogt, S. S., Laughlin, G., et al. 2017, *AJ*, 153, 208, doi: [10.3847/1538-3881/aa66ca](https://doi.org/10.3847/1538-3881/aa66ca)
- Carretta, E. 2013, *A&A*, 557, A128, doi: [10.1051/0004-6361/201322103](https://doi.org/10.1051/0004-6361/201322103)
- Casagrande, L., Schönrich, R., Asplund, M., et al. 2011, *A&A*, 530, A138, doi: [10.1051/0004-6361/201016276](https://doi.org/10.1051/0004-6361/201016276)
- Catanzarite, J., Law, N., & Shao, M. 2008, in *Society of Photo-Optical Instrumentation Engineers (SPIE) Conference Series*, Vol. 7013, *Optical and Infrared Interferometry*, ed. M. Schöller, W. C. Danchi, & F. Delplancke, 70132K, doi: [10.1117/12.787904](https://doi.org/10.1117/12.787904)
- Chiavassa, A., Caldas, A., Selsis, F., et al. 2017, *A&A*, 597, A94, doi: [10.1051/0004-6361/201528018](https://doi.org/10.1051/0004-6361/201528018)
- Chulkov, D., & Malkov, O. 2022, *MNRAS*, 517, 2925, doi: [10.1093/mnras/stac2827](https://doi.org/10.1093/mnras/stac2827)
- Claret, A. 2000, *A&A*, 363, 1081
- . 2018, *A&A*, 618, A20, doi: [10.1051/0004-6361/201833060](https://doi.org/10.1051/0004-6361/201833060)
- Clayton, Z. R., van Saders, J. L., Llama, J., et al. 2022, *ApJ*, 927, 219, doi: [10.3847/1538-4357/ac498f](https://doi.org/10.3847/1538-4357/ac498f)
- Cvetkovic, Z., & Ninkovic, S. 2010, *Serbian Astronomical Journal*, 180, 71, doi: [10.2298/SAJ1080071C](https://doi.org/10.2298/SAJ1080071C)
- Duncan, D. K., Vaughan, A. H., Wilson, O. C., et al. 1991, *ApJS*, 76, 383, doi: [10.1086/191572](https://doi.org/10.1086/191572)
- Eriksson, U., & Lindegren, L. 2007, *A&A*, 476, 1389, doi: [10.1051/0004-6361:20078031](https://doi.org/10.1051/0004-6361:20078031)
- Forgács-Dajka, E., Dobos, L., & Ballai, I. 2021, *A&A*, 653, A50, doi: [10.1051/0004-6361/202140731](https://doi.org/10.1051/0004-6361/202140731)
- Gaia Collaboration, Arenou, F., Babusiaux, C., et al. 2023, *A&A*, 674, A34, doi: [10.1051/0004-6361/202243782](https://doi.org/10.1051/0004-6361/202243782)
- Gandhi, P., Dashwood Brown, C., Zhao, Y., et al. 2023, *arXiv e-prints*, arXiv:2306.16479, doi: [10.48550/arXiv.2306.16479](https://doi.org/10.48550/arXiv.2306.16479)
- Gilbertson, C., Ford, E. B., & Dumusque, X. 2020, *Research Notes of the American Astronomical Society*, 4, 59, doi: [10.3847/2515-5172/ab8d44](https://doi.org/10.3847/2515-5172/ab8d44)
- Gomes da Silva, J., Santos, N. C., Adibekyan, V., et al. 2021, *A&A*, 646, A77, doi: [10.1051/0004-6361/202039765](https://doi.org/10.1051/0004-6361/202039765)
- Gray, R. O., Corbally, C. J., Garrison, R. F., et al. 2006, *AJ*, 132, 161, doi: [10.1086/504637](https://doi.org/10.1086/504637)
- Hardegree-Ullman, K. K., Apai, D., Bergsten, G. J., Pascucci, I., & López-Morales, M. 2023, *AJ*, 165, 267, doi: [10.3847/1538-3881/acd1ec](https://doi.org/10.3847/1538-3881/acd1ec)
- Hatzes, A. P. 2002, *Astronomische Nachrichten*, 323, 392, doi: [10.1002/1521-3994\(200208\)323:3/4<392::AID-ASNA392>3.0.CO;2-M](https://doi.org/10.1002/1521-3994(200208)323:3/4<392::AID-ASNA392>3.0.CO;2-M)
- Henry, T. J., Soderblom, D. R., Donahue, R. A., & Baliunas, S. L. 1996, *AJ*, 111, 439, doi: [10.1086/117796](https://doi.org/10.1086/117796)
- Hirsch, L. A., Rosenthal, L., Fulton, B. J., et al. 2021, *AJ*, 161, 134, doi: [10.3847/1538-3881/abd639](https://doi.org/10.3847/1538-3881/abd639)
- Hojjatpanah, S., Figueira, P., Santos, N. C., et al. 2019, *A&A*, 629, A80, doi: [10.1051/0004-6361/201834729](https://doi.org/10.1051/0004-6361/201834729)
- Hojjatpanah, S., Oshagh, M., Figueira, P., et al. 2020, *A&A*, 639, A35, doi: [10.1051/0004-6361/202038035](https://doi.org/10.1051/0004-6361/202038035)
- Holmberg, J., Nordström, B., & Andersen, J. 2009, *A&A*, 501, 941, doi: [10.1051/0004-6361/200811191](https://doi.org/10.1051/0004-6361/200811191)
- Horne, J. H., & Baliunas, S. L. 1986, *ApJ*, 302, 757, doi: [10.1086/164037](https://doi.org/10.1086/164037)
- Houdebine, É. R., Mullan, D. J., Doyle, J. G., et al. 2019, *AJ*, 158, 56, doi: [10.3847/1538-3881/ab23fe](https://doi.org/10.3847/1538-3881/ab23fe)
- Howard, R. F. 1992, *SoPh*, 137, 51, doi: [10.1007/BF00146575](https://doi.org/10.1007/BF00146575)
- Huang, P., Dong, R., Li, H., Li, S., & Ji, J. 2019, *ApJL*, 883, L39, doi: [10.3847/2041-8213/ab40c4](https://doi.org/10.3847/2041-8213/ab40c4)
- Huang, X., & Ji, J. 2022, *AJ*, 164, 177, doi: [10.3847/1538-3881/ac8f4c](https://doi.org/10.3847/1538-3881/ac8f4c)
- Huang, X., Ji, J., Liu, S., Dong, R., & Wang, S. 2023, *ApJ*, 956, 45, doi: [10.3847/1538-4357/acf46e](https://doi.org/10.3847/1538-4357/acf46e)
- Hunter, J. D. 2007, *Computing in Science and Engineering*, 9, 90, doi: [10.1109/MCSE.2007.55](https://doi.org/10.1109/MCSE.2007.55)

- Ida, S., & Lin, D. N. C. 2004, *ApJ*, 604, 388, doi: [10.1086/381724](https://doi.org/10.1086/381724)
- Irving, Z. A., Saar, S. H., Wargelin, B. J., & do Nascimento, J.-D. 2023, *ApJ*, 949, 51, doi: [10.3847/1538-4357/acc468](https://doi.org/10.3847/1538-4357/acc468)
- Isaacson, H., & Fischer, D. 2010, *ApJ*, 725, 875, doi: [10.1088/0004-637X/725/1/875](https://doi.org/10.1088/0004-637X/725/1/875)
- Ji, J., Tan, D., Bao, C., et al. 2023, *Research in Astronomy and Astrophysics*, 23, 125015, doi: [10.1088/1674-4527/ad0499](https://doi.org/10.1088/1674-4527/ad0499)
- Ji, J.-H., Li, H.-T., Zhang, J.-B., et al. 2022, *Research in Astronomy and Astrophysics*, 22, 072003, doi: [10.1088/1674-4527/ac77e4](https://doi.org/10.1088/1674-4527/ac77e4)
- Jin, M., Fu, J., Wang, J., & Zong, W. 2023, *Universe*, 9, 417, doi: [10.3390/universe9090417](https://doi.org/10.3390/universe9090417)
- Jin, S., Ding, X., Wang, S., Dong, Y., & Ji, J. 2022, *MNRAS*, 509, 4608, doi: [10.1093/mnras/stab3317](https://doi.org/10.1093/mnras/stab3317)
- Jin, S., Li, S., Isella, A., Li, H., & Ji, J. 2016, *ApJ*, 818, 76, doi: [10.3847/0004-637X/818/1/76](https://doi.org/10.3847/0004-637X/818/1/76)
- Jin, S., Mordasini, C., Parmentier, V., et al. 2014, *ApJ*, 795, 65, doi: [10.1088/0004-637X/795/1/65](https://doi.org/10.1088/0004-637X/795/1/65)
- Jofré, E., Petrucci, R., Saffe, C., et al. 2015, *A&A*, 574, A50, doi: [10.1051/0004-6361/201424474](https://doi.org/10.1051/0004-6361/201424474)
- Johansen, A., Oishi, J. S., Mac Low, M.-M., et al. 2007, *Nature*, 448, 1022, doi: [10.1038/nature06086](https://doi.org/10.1038/nature06086)
- Johnson, L. J., Norris, C. M., Unruh, Y. C., et al. 2021, *MNRAS*, 504, 4751, doi: [10.1093/mnras/stab1190](https://doi.org/10.1093/mnras/stab1190)
- Jurgenson, C., Fischer, D., McCracken, T., et al. 2016, in *Society of Photo-Optical Instrumentation Engineers (SPIE) Conference Series*, Vol. 9908, *Ground-based and Airborne Instrumentation for Astronomy VI*, ed. C. J. Evans, L. Simard, & H. Takami, 99086T, doi: [10.1117/12.2233002](https://doi.org/10.1117/12.2233002)
- Kaplan-Lipkin, A., Macintosh, B., Madurowicz, A., et al. 2022, *AJ*, 163, 205, doi: [10.3847/1538-3881/ac56e0](https://doi.org/10.3847/1538-3881/ac56e0)
- Kawata, D., Kawahara, H., Gouda, N., et al. 2023, *arXiv e-prints*, arXiv:2307.05666, doi: [10.48550/arXiv.2307.05666](https://doi.org/10.48550/arXiv.2307.05666)
- Kopparapu, R. K., Ramirez, R. M., SchottelKotte, J., et al. 2014, *ApJL*, 787, L29, doi: [10.1088/2041-8205/787/2/L29](https://doi.org/10.1088/2041-8205/787/2/L29)
- Lagrange, A. M., Desort, M., & Meunier, N. 2010, *A&A*, 512, A38, doi: [10.1051/0004-6361/200913071](https://doi.org/10.1051/0004-6361/200913071)
- Lagrange, A. M., Meunier, N., Desort, M., & Malbet, F. 2011, *A&A*, 528, L9, doi: [10.1051/0004-6361/201016354](https://doi.org/10.1051/0004-6361/201016354)
- Lalot, K., Burt, J. A., Mamajek, E. E., et al. 2023, *AJ*, 165, 176, doi: [10.3847/1538-3881/acc067](https://doi.org/10.3847/1538-3881/acc067)
- Lanza, A. F., Pagano, I., Leto, G., et al. 2009, *A&A*, 493, 193, doi: [10.1051/0004-6361:200810591](https://doi.org/10.1051/0004-6361:200810591)
- Latković, O., Čeki, A., & Lazarević, S. 2021, *ApJS*, 254, 10, doi: [10.3847/1538-4365/abeb23](https://doi.org/10.3847/1538-4365/abeb23)
- Lightkurve Collaboration, Cardoso, J. V. d. M., Hedges, C., et al. 2018, *Lightkurve: Kepler and TESS time series analysis in Python*, *Astrophysics Source Code Library*, record ascl:1812.013. <http://ascl.net/1812.013>
- Lin, A. S. J., Monson, A., Mahadevan, S., et al. 2022, *AJ*, 163, 184, doi: [10.3847/1538-3881/ac5622](https://doi.org/10.3847/1538-3881/ac5622)
- Liu, B., & Ji, J. 2020, *Research in Astronomy and Astrophysics*, 20, 164, doi: [10.1088/1674-4527/20/10/164](https://doi.org/10.1088/1674-4527/20/10/164)
- Liu, B., Lambrechts, M., Johansen, A., & Liu, F. 2019, *A&A*, 632, A7, doi: [10.1051/0004-6361/201936309](https://doi.org/10.1051/0004-6361/201936309)
- Luck, R. E. 2017, *AJ*, 153, 21, doi: [10.3847/1538-3881/153/1/21](https://doi.org/10.3847/1538-3881/153/1/21)
- Luck, R. E., & Heiter, U. 2006, *AJ*, 131, 3069, doi: [10.1086/504080](https://doi.org/10.1086/504080)
- Makarov, V. V., Beichman, C. A., Catanzarite, J. H., et al. 2009, *ApJL*, 707, L73, doi: [10.1088/0004-637X/707/1/L73](https://doi.org/10.1088/0004-637X/707/1/L73)
- Makarov, V. V., Parker, D., & Ulrich, R. K. 2010, *ApJ*, 717, 1202, doi: [10.1088/0004-637X/717/2/1202](https://doi.org/10.1088/0004-637X/717/2/1202)
- Mamajek, E., & Stapelfeldt, K. 2024, *arXiv e-prints*, arXiv:2402.12414, doi: [10.48550/arXiv.2402.12414](https://doi.org/10.48550/arXiv.2402.12414)
- Mamajek, E. E., & Hillenbrand, L. A. 2008, *ApJ*, 687, 1264, doi: [10.1086/591785](https://doi.org/10.1086/591785)
- McQuillan, A., Mazeh, T., & Aigrain, S. 2014, *ApJS*, 211, 24, doi: [10.1088/0067-0049/211/2/24](https://doi.org/10.1088/0067-0049/211/2/24)
- Meunier, N., & Lagrange, A. M. 2022, *A&A*, 659, A104, doi: [10.1051/0004-6361/202142702](https://doi.org/10.1051/0004-6361/202142702)
- Meunier, N., Lagrange, A. M., & Borgniet, S. 2020, *A&A*, 644, A77, doi: [10.1051/0004-6361/202038710](https://doi.org/10.1051/0004-6361/202038710)
- Meunier, N., Lagrange, A. M., Boulet, T., & Borgniet, S. 2019, *A&A*, 627, A56, doi: [10.1051/0004-6361/201834796](https://doi.org/10.1051/0004-6361/201834796)
- Meunier, N., Pous, R., Sulis, S., Mary, D., & Lagrange, A. M. 2023, *A&A*, 676, A82, doi: [10.1051/0004-6361/202346218](https://doi.org/10.1051/0004-6361/202346218)
- Mordasini, C., Alibert, Y., Klahr, H., & Henning, T. 2012, *A&A*, 547, A111, doi: [10.1051/0004-6361/201118457](https://doi.org/10.1051/0004-6361/201118457)
- Morris, B. M., Agol, E., Davenport, J. R. A., & Hawley, S. L. 2018, *MNRAS*, 476, 5408, doi: [10.1093/mnras/sty568](https://doi.org/10.1093/mnras/sty568)
- Morris, B. M., Bobra, M. G., Agol, E., Lee, Y. J., & Hawley, S. L. 2020, *MNRAS*, 493, 5489, doi: [10.1093/mnras/staa618](https://doi.org/10.1093/mnras/staa618)
- Namekata, K., Maehara, H., Notsu, Y., et al. 2019, *ApJ*, 871, 187, doi: [10.3847/1538-4357/aaf471](https://doi.org/10.3847/1538-4357/aaf471)
- Nielsen, M. B., Gizon, L., Cameron, R. H., & Miesch, M. 2019, *A&A*, 622, A85, doi: [10.1051/0004-6361/201834373](https://doi.org/10.1051/0004-6361/201834373)
- Norris, C. 2019, PhD thesis, Imperial College London
- Norris, C. M., Unruh, Y. C., Witzke, V., et al. 2023, *MNRAS*, 524, 1139, doi: [10.1093/mnras/stad1738](https://doi.org/10.1093/mnras/stad1738)

- Noyes, R. W., Weiss, N. O., & Vaughan, A. H. 1984, *ApJ*, 287, 769, doi: [10.1086/162735](https://doi.org/10.1086/162735)
- Pace, G. 2013, *A&A*, 551, L8, doi: [10.1051/0004-6361/201220364](https://doi.org/10.1051/0004-6361/201220364)
- Paegert, M., Stassun, K. G., Collins, K. A., et al. 2021, arXiv e-prints, arXiv:2108.04778, doi: [10.48550/arXiv.2108.04778](https://doi.org/10.48550/arXiv.2108.04778)
- Paletou, F., Böhm, T., Watson, V., & Trouilhet, J. F. 2015, *A&A*, 573, A67, doi: [10.1051/0004-6361/201424741](https://doi.org/10.1051/0004-6361/201424741)
- Pan, M., Wang, S., & Ji, J. 2022, *MNRAS*, 510, 4134, doi: [10.1093/mnras/stab3611](https://doi.org/10.1093/mnras/stab3611)
- Pan, M., Liu, B., Johansen, A., et al. 2024, *A&A*, 682, A89, doi: [10.1051/0004-6361/202347664](https://doi.org/10.1051/0004-6361/202347664)
- Pan, Y., Fu, J.-N., Zong, W., et al. 2020, *ApJ*, 905, 67, doi: [10.3847/1538-4357/abc250](https://doi.org/10.3847/1538-4357/abc250)
- Pepe, F. A., Cristiani, S., Rebolo Lopez, R., et al. 2010, in *Society of Photo-Optical Instrumentation Engineers (SPIE) Conference Series*, Vol. 7735, *Ground-based and Airborne Instrumentation for Astronomy III*, ed. I. S. McLean, S. K. Ramsay, & H. Takami, 77350F, doi: [10.1117/12.857122](https://doi.org/10.1117/12.857122)
- Perdigon, J., de Laverny, P., Recio-Blanco, A., et al. 2021, *A&A*, 647, A162, doi: [10.1051/0004-6361/202040147](https://doi.org/10.1051/0004-6361/202040147)
- Perrin, M. N., Cayrel de Strobel, G., & Dennefeld, M. 1988, *A&A*, 191, 237
- Perryman, M., Hartman, J., Bakos, G. Á., & Lindegren, L. 2014, *ApJ*, 797, 14, doi: [10.1088/0004-637X/797/1/14](https://doi.org/10.1088/0004-637X/797/1/14)
- Ramírez, I., Allende Prieto, C., & Lambert, D. L. 2013, *ApJ*, 764, 78, doi: [10.1088/0004-637X/764/1/78](https://doi.org/10.1088/0004-637X/764/1/78)
- Reiners, A., & Zechmeister, M. 2020, *ApJS*, 247, 11, doi: [10.3847/1538-4365/ab609f](https://doi.org/10.3847/1538-4365/ab609f)
- Reinhold, T., & Hekker, S. 2020, *A&A*, 635, A43, doi: [10.1051/0004-6361/201936887](https://doi.org/10.1051/0004-6361/201936887)
- Shapiro, A. I., Solanki, S. K., & Krivova, N. A. 2021, *ApJ*, 908, 223, doi: [10.3847/1538-4357/abd630](https://doi.org/10.3847/1538-4357/abd630)
- Solanki, S. K. 2003, *A&A Rv*, 11, 153, doi: [10.1007/s00159-003-0018-4](https://doi.org/10.1007/s00159-003-0018-4)
- Solanki, S. K., & Unruh, Y. C. 2004, *MNRAS*, 348, 307, doi: [10.1111/j.1365-2966.2004.07368.x](https://doi.org/10.1111/j.1365-2966.2004.07368.x)
- Soubiran, C., Brouillet, N., & Casamiquela, L. 2022, *A&A*, 663, A4, doi: [10.1051/0004-6361/202142409](https://doi.org/10.1051/0004-6361/202142409)
- Sowmya, K., Némec, N. E., Shapiro, A. I., et al. 2022, *ApJ*, 934, 146, doi: [10.3847/1538-4357/ac79b3](https://doi.org/10.3847/1538-4357/ac79b3)
- . 2021, *ApJ*, 919, 94, doi: [10.3847/1538-4357/ac111b](https://doi.org/10.3847/1538-4357/ac111b)
- Stassun, K. G., Oelkers, R. J., Paegert, M., et al. 2019, *AJ*, 158, 138, doi: [10.3847/1538-3881/ab3467](https://doi.org/10.3847/1538-3881/ab3467)
- Staude, J., Rendtel, J., Balthasar, H., & Zhugzhda, Y. 1999, in *ESA Special Publication*, Vol. 448, *Magnetic Fields and Solar Processes*, ed. A. Wilson & et al., 373
- Steinmetz, M., Guiglion, G., McMillan, P. J., et al. 2020, *AJ*, 160, 83, doi: [10.3847/1538-3881/ab9ab8](https://doi.org/10.3847/1538-3881/ab9ab8)
- Strassmeier, K. G. 2009, *A&A Rv*, 17, 251, doi: [10.1007/s00159-009-0020-6](https://doi.org/10.1007/s00159-009-0020-6)
- Suárez Mascareño, A., Rebolo, R., & González Hernández, J. I. 2016, *A&A*, 595, A12, doi: [10.1051/0004-6361/201628586](https://doi.org/10.1051/0004-6361/201628586)
- Sulis, S., Lendl, M., Cegla, H. M., et al. 2023, *A&A*, 670, A24, doi: [10.1051/0004-6361/202244223](https://doi.org/10.1051/0004-6361/202244223)
- Terrien, R. C., Mahadevan, S., Deshpande, R., & Bender, C. F. 2015, *ApJS*, 220, 16, doi: [10.1088/0067-0049/220/1/16](https://doi.org/10.1088/0067-0049/220/1/16)
- The Theia Collaboration, Boehm, C., Krone-Martins, A., et al. 2017, arXiv e-prints, arXiv:1707.01348, doi: [10.48550/arXiv.1707.01348](https://doi.org/10.48550/arXiv.1707.01348)
- Thiele, T. N. 1883, *Astronomische Nachrichten*, 104, 245
- Unwin, S. C., Shao, M., Tanner, A. M., et al. 2008, *PASP*, 120, 38, doi: [10.1086/525059](https://doi.org/10.1086/525059)
- Virtanen, P., Gommers, R., Oliphant, T. E., et al. 2020, *Nature Methods*, 17, 261, doi: [10.1038/s41592-019-0686-2](https://doi.org/10.1038/s41592-019-0686-2)
- Vogt, S. S., & Penrod, G. D. 1983, *PASP*, 95, 565, doi: [10.1086/131208](https://doi.org/10.1086/131208)
- Witzke, V., Reinhold, T., Shapiro, A. I., Krivova, N. A., & Solanki, S. K. 2020, *A&A*, 634, L9, doi: [10.1051/0004-6361/201936608](https://doi.org/10.1051/0004-6361/201936608)
- Wright, J. T., Marcy, G. W., Butler, R. P., & Vogt, S. S. 2004, *ApJS*, 152, 261, doi: [10.1086/386283](https://doi.org/10.1086/386283)
- Yang, Z., Zhang, L., Meng, G., et al. 2023, *A&A*, 669, A15, doi: [10.1051/0004-6361/202142710](https://doi.org/10.1051/0004-6361/202142710)
- Youdin, A. N., & Goodman, J. 2005, *ApJ*, 620, 459, doi: [10.1086/426895](https://doi.org/10.1086/426895)
- Zhao, L. L., Fischer, D. A., Ford, E. B., et al. 2022, *AJ*, 163, 171, doi: [10.3847/1538-3881/ac5176](https://doi.org/10.3847/1538-3881/ac5176)
- Zong, W., Fu, J.-N., De Cat, P., et al. 2018, *ApJS*, 238, 30, doi: [10.3847/1538-4365/aadf81](https://doi.org/10.3847/1538-4365/aadf81)